RESEARCH PAPER

Effect of active mixing on capture efficiency in heterogeneous microfluidic immunosensor

Shipra Verma[1,2] · Siddhartha Panda[1,2,3]

Abstract

The enhanced capture of the antigen (Ag) by the surface-immobilized antibodies (Ab) in heterogeneous microfluidic immunosensors lowers (improves) the detection limit thus facilitating the early disease detection. The efficient capture of the antigen is subjected to the interaction of the transport parameters, reaction parameters and the microfluidic system geometry. In the present work, the role of active mixing in facilitating the transport in flow-based heterogeneous immunosensor was studied, both numerically and experimentally. The experiments were performed with the capture of prostate-specific antigen (PSA) by *anti*-PSA and the results were validated using numerical simulations. The average Sherwood number (Sh) for the experiments and simulations was comparable. First, the effect of the nature of the flow on the capture efficiency was tested, which showed the enhancement in the antigen capture using active mixing. Further, studies of individual active mixing parameter (average velocity, frequency and amplitude) on analyte capture were conducted. The increase in average velocity (u_{avg}) increases the antigen capture but the corresponding pressure drop also increases, and the figure of merit (FOM) attains a maximum at $Re \sim 0.6$. Similar behavior was observed with the increase of the frequency. The continuous increase in the frequency reduces the reaction time scale and decreases the analyte capture. The amplitude has the least effect on the antigen capture. The flow profiles were also seen and the temporal variation was compared at different flow conditions with micro-PIV. We also proposed two correlations utilizing the parameters—the average surface concentration ($C_{s,avg}$), the Reynolds number (Re) and the Strouhal number (St). The correlations indicate that the dependency coefficient for St is higher than Re, and signify the impact of vortex propagation (i.e., active mixing) on antigen capture.

Keywords Capture efficiency · Transport · Active mixing · Microfluidic immunosensing

1 Introduction

Microfluidic immunosensors have attracted great interest for point-of-care applications. The beneficial features of microfluidic devices include a high surface area–volume

✉ Siddhartha Panda
spanda@iitk.ac.in

1   Department of Chemical Engineering, Indian Institute of Technology Kanpur, Kanpur, India

2   Samtel Centre for Display Technologies, Indian Institute of Technology Kanpur, Kanpur, India

3   National Centre for Flexible Electronics, Indian Institute of Technology Kanpur, Kanpur, UP 208016, India

ratio, reduced reagent consumption, short analysis times, and high efficiency. In a flow-based microfluidic immunosensor, antibodies (Ab) are immobilized on the channel walls via intermediate linkers, and antigens (Ag) are transported from the bulk solution to the surface of the microchannel to react with and be captured by the *Ab*. An important performance parameter is the "*capture efficiency*", which is defined as the ratio of the number of antigens captured to the maximum available antibodies on the surface of the immunosensor (Rath and Panda 2012, 2015; Verma and Panda 2020). High capture efficiency will reduce (and, thus, improve) the limit of detection and, thus, facilitate early detection of disease. It can be improved either by increasing the *Ab* density on the surface of the immunosensor or by facilitating *Ag* transport. A significant body of research exists that uses physical (Rath and Panda 2012) and chemical (Rath and Panda 2015, 2016; Chepyala and Panda 2013, 2014; Vijayendran and Leckband 2001; Squires et al. 2008; Hu et al. 2007;

Nelson et al. 2007; Reverberi and Reverberi 2007; Lebedev et al. 2006; Ibii et al. 2010) methods to increase the antibody density by modifying the surface of an immunosensor. Both active and passive mixers have been designed to facilitate the *Ag* transport to the channel walls.

For immunosensing (Wang et al. 1998; Fujii et al. 2003; Renaudin et al. 2010; Hart et al. 2010; Sarvazyan 2010; Kardous et al. 2011; Yu et al. 2015; Chen et al. 2016) and non-immunosensing (Bange et al. 2005; Hessel et al. 2005; Nguyen and Wu 2005; Lee et al. 2011; Mansur et al. 2008; Asgharzadehahmadi et al. 2016) applications, active mixing can be achieved using different forms of external energy inputs, such as acoustic-induced vibrations, electrokinetic instabilities, periodic variation of pumping capacity, small impellers, and integrated micro-valves or micro-pumps. Several researchers (Abbott et al. 2012, 2014) have demonstrated active mixing processes that utilize constant flow and moving geometry to increase mass transfer (i.e., improving the detection limit) and have the ability to be scaled up (oscillatory flow and oscillatory baffled reactors). Another approach is to utilize the pulse mode for the inlet velocity. The parameters of active mixing include velocity, frequency, and amplitude of the mixing pulse. Fujii et al. (2003) achieved better mixing performance using a pulsed flow and demonstrated the effect of frequency (switching frequency of pump) on immunosensing. To analyze the unsteady and oscillating behavior of fluid flow, the dimensionless number, *Strouhal number (St)* (which measures the effective vortex propagation and mixing intensity) is used. St ($St = (L/V)/(1/f)$, Chen and Cho (2008)) is defined as the ratio of the characteristic flow time (L/V) to the pulsing time period ($1/f$), where L is the characteristic length, V is the average flow velocity, and f is the frequency of oscillation. However, the effect of pulsing in a microfluidic immunosensor, which includes the individual effects of all the governing parameters for immunosensing surface reactions, along with the correlation between the average surface concentration and process parameters has not been reported till date. Therefore, in the present study, we obtain the optimum process parameters and a *figure of merit* for a given system. A knowledge of flow patterns and mixing behavior is important when selecting an appropriate reactor design.

In this work, the effect of active mixing by means of pulse flow was analysed, both numerically and experimentally, along with the effect of the governing parameters (frequency, amplitude and velocity) on the capture efficiency for flow-based heterogeneous immunosensors. The experiments were performed to provide empirical validation of the simulation results (similar geometrical and process parameters could not be taken due to fabrication and computational limitations). A square wave was utilized for the simulation, and the effects of the governing parameters were studied using a convection–diffusion–reaction model. From this,

dependence of the governing parameters on the transport and reaction parameters was obtained. Variation in any of the parameters affects the flow profile and *Ag* transport. Few experiments were conducted for detecting prostate-specific antigen (PSA) molecules to verify whether active mixing improved *Ag* transport and enhanced the extent of the reaction. Cyclic voltammetry (CV) peaks were used to quantify the presence of biomolecules in the experimental system. For flow visualization at different flow conditions, the positions of the streamlines were captured with the help of particle image velocimetry (micro-PIV).

2 Simulations and experiments

2.1 Simulation technique

The procedure for simulating the transport of the antigen (*Ag*) and capture by the antibody (*Ab*) is governed by the equations mentioned in the next Sect. 2.1.1. The computational method employed here made use of the finite element method (FEM) using COMSOL multiphysics software. The required modules were the "Navier–Stokes equations", "transport of dilute species" and "surface reactions". We have utilized piecewise function to define velocity (pulse form) for different cases. The PARDISO solver was used to solve all the modules. The straight microchannel of dimensions 3 mm × 800 μm × 50 μm was used for simulation study. We could not go beyond a channel length of 3 mm due to computational limitations. The studied geometry consisted of 173,238 number of elements. The computation times for the fluid flow and the transport of the dilute species were 20 s (total time) in intervals of 0.1 s; while for the surface reaction, it was 20 s in intervals of 0.01 s. The validity of the outflow boundary conditions was checked.

2.1.1 Governing equations

The transport of *Ag* to the *Ab* has been described by (Rath and Panda 2012):

$$\frac{\partial C}{\partial t} = D.\nabla^2 C - u.\nabla C$$

(Fick's Law for concentration field of a dilute solvent),

(1)

$$B - \frac{1}{\rho}\nabla.P + \nu.\nabla^2 V = \frac{DV}{Dt}$$

(2)

(Navier-Stokes equation (conservation of momentum)),

$$\frac{\partial u}{\partial x} + \frac{\partial v}{\partial y} + \frac{\partial w}{\partial z} = 0 \quad \text{(Continuity equation (conservation of mass))},$$

(3)

$$\frac{d\theta_t}{dt} = K_{on}C(z=0,x,y,t)\left(\theta_{max} - \theta_t\right) - K_{off}\theta_t, \tag{4}$$

where C is the analyte concentration at time t, D is the diffusivity of the antigens in the solution flowing in the microchannels, u, v, and w are the velocity components in the x, y and z directions, respectively, B is the body force, $\nabla.P$ is the pressure gradient, θ_t is the surface density of antigen–antibody bound complex at time t, θ_{max} is the maximum surface density of the immobilized antibodies, and K_{on} and K_{off} are the forward and backward rate constants, respectively, h is the channel height, w is the channel width. The schematic of the computational domain is shown in Fig. 1a with the schematic information provided below.

The microchannel dimensions (shown in Fig. 1a) are $3\text{ mm} \times 800\text{ μm} \times 50\text{ μm}$; u, v, and w are the velocity components in the x, y and z directions, respectively (shown in the schematic); inlet plane: ABCD, outlet plane: EFGH, channel reactive surface or plane: BCGF.

The initial and boundary conditions for the above equations are given by (Rath and Panda 2012):

$$C(x,y,z,t=0) = 0, \tag{5}$$

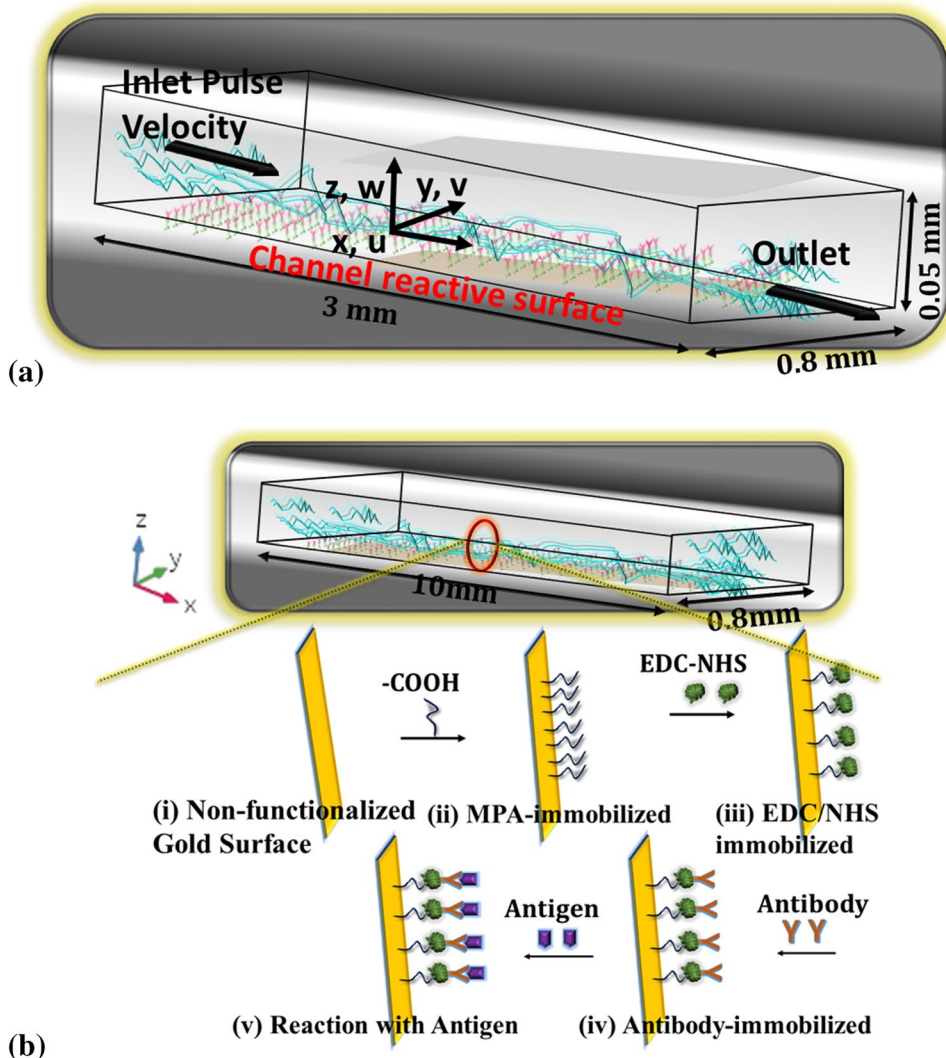$$u,v,w(t=0) = 0, \tag{6}$$

$$C_i(x,y,z,t) = C_b \quad (C_b = \text{bulk concentration, at outlet } D_i\nabla C_i = 0), \tag{7}$$

$$D\frac{\partial C(z=0,x,y,t)}{\partial x} = K_{on}C(z=0,x,y,t)\left(\theta_{max} - \theta_t\right) - K_{off}\theta_t, \tag{8}$$

$$D\frac{\partial C(z=h,x,y,t)}{\partial x} = 0, \tag{9}$$

Fig. 1 **a** Schematic of the computational domain. (Dimensions shown are not to scale). **b** Schematic of the stack immobilization process for the capture of PSA by anti-PSA on the gold surface of the microchannel (Dimensions shown are not to scale)

$$D\frac{\partial C(z, x, y = 0, t)}{\partial x} = 0, \tag{10}$$

$$D\frac{\partial C(z, x, y = \mathrm{w}, t)}{\partial x} = 0, \tag{11}$$

$$\theta_t(t = 0) = 0.$$

The velocity equation is given (From *MathWorld*) by:

$$v(t) = A_0 + j(x),$$
$$j(x) = A.pw(t),$$

$$\text{where} \quad pw(t) = \begin{cases} -1, x - x_0 < 0 \\ 0, x - x_0 = 0 \\ 1, x - x_0 > 0 \end{cases} \tag{12}$$

where A_0 and A are constant and x_0 varies with the parameters.

The dimensionless numbers,

the Reynolds number, $\quad Re = \dfrac{D_h u_{avg} \rho}{\mu}, \tag{13}$

the Reynolds number of the oscillation, $\quad Re_o = \dfrac{2\pi f A D \rho}{\mu}, \tag{14}$

and the Strouhal number, $\quad St = \dfrac{(L/u_{avg})}{\left(\frac{1}{f}\right)} = \dfrac{Lf}{u_{avg}}, \tag{15}$

are used in this study, where D_h = hydraulic diameter of the channel, u_{avg} = average inlet flow velocity, μ = viscosity, A = center to peak amplitude of the oscillation, and f = frequency of the oscillation.

To check the applicability of the outflow boundary conditions, we calculated the entrance length (L_h) for the geometry (hydraulic diameter, $D = 94$ μm) and flow ($Re = 1.2$) at constant flow (no pulse) to be about 7 μm (which far less than the channel length of 3 mm). The St considered here is small (i.e., of the order 10^{-3}) in this study and the generated perturbations are also smaller/lower. Thus, we believe that the use of the outflow boundary conditions is reasonable.

The values of the input parameters were taken from the range defined in the literature (Rath and Panda 2012, 2015; Verma and Panda 2020) and are mentioned in Table 1:

2.2 Chemicals

All chemicals and experimental steps are nearly the same as mentioned in our earlier work (Verma and Panda 2020). Briefly, Mercapto propionic acid (MPA) and EDC-NHS

Table 1 Input parameters used in the COMSOL simulations

Parameters	Value(s)
K_D	$10^{-6}\ M$
K_{on}	$10^{+3}\ \mathrm{M}^{-1}\mathrm{s}^{-1}$
K_{off}	$10^{-3}\ \mathrm{s}^{-1}$
D	$3.7 \times 10^{-11}\ \mathrm{m}^2/\mathrm{s}$
C_b	$1.0 \times 10^{-6}\ \mathrm{mol/m}^3$
θ_{max}	$1.68 \times 10^{-7}\ \mathrm{mol/m}^2$

were obtained from Sigma Aldrich (Germany) and Merck (Germany) respectively; isopropanol (IPA) was obtained from Loba Chemie (India); potassium ferricyanide and potassium ferrocyanide were obtained from Rankem (India). The components required for the PBS solution (KCl, NaCl, Na_2HPO_4, and KH_2PO_4) were purchased from Qualigens (India); the pH of PBS for all the experiments was maintained at 7.4. PDMS and glass slides were obtained from SYLGARD 184 (Dow Corning, USA), and Bioplus (India), respectively; SU-8 2050 epoxy for moulds fabrication was purchased from MicroChem Corporation (USA); prostate-specific antigen (PSA) was obtained from Fitzgerald Industries International (USA), anti-PSA antibodies were purchased from Genetech Laboratory (India), and silicon wafers ((100), surface roughness < 2 nm) were purchased from Wafer World (USA).

2.3 Channel fabrication

Glass-PDMS (Srivastava et al. 2011; Zhang et al. 2015; Chen et al. 2019; Meng-Di et al. 2019) straight microchannels of dimensions 10 mm × 800 μm × 50 μm were used in this study. The glass-PDMS microchannel fabrication protocol is the same as mentioned in our earlier work (Verma and Panda 2020). Briefly, all the fabrication steps were processed in a controlled clean room environment. Glass slides were cleaned using piranha solution and followed by the deposition of chromium (10 nm) and gold (90 nm) by means of thermal deposition. Masks used for metal deposition as well as epoxy moulds were fabricated using a laser system (Nd:YAG Laser, Laservall, Italy). PDMS flow channels were made (Di et al. 2019; Art et al. 2018; Kadilak et al. 2014; Fujii 2002) using the SU-8 epoxy. For epoxy moulds fabrication, epoxy was spin coated on silicon for consecutive steps at 500 and 2500 RPM for 10 and 45 s, respectively. The spun epoxy was prebaked at 95 °C for 7 min, exposed for 8 min to a 240 mJ/cm² UV lamp with a copper mask, followed by baking of 7 min at 95 °C. The baked epoxy was developed in 7 min using the SU-8 developer and followed by rinsing with a fresh developer (for 10 s) and IPA (for 15 s). Further, the PDMS mixture was prepared (base and cross linker) in 10:1 ratio (by weight), degassed, poured over the epoxy moulds, and was heated for 1 h at 70–72 °C, in vacuum. This was cooled down up to room temperature

and the microchannel was separated out from the mould. The inlet/outlet ports were drilled on the PDMS microchannel before being bonded to the glass slide (on which the gold was deposited). The oxygen plasma method was used to bond channels. In the above-described way, the microchannels were fabricated. We used the similar glass-PDMS microchannel for the micro-PIV study, without a gold layer to observe the flow profile directly as the gold layer blocked optical assessment of the flow profile.

2.4 Channel functionalization

All the process steps for stack immobilization and functionalization, utilizing processes described in the literature (Verma and Panda 2020; Bhuvana et al. 2013) are shown in (Fig. 1(b)(i)–1(b)(v)). Briefly, the non-functionalized microchannel was washed with ultrapure water and then dried with nitrogen followed by incubating the channel surface (gold surface) in a 1-mM MPA solution (PBS solution) for 2 h and washing with PBS. The terminal carboxylic acid (–COOH) groups were activated, followed by immobilization of 0.2 M NHS/0.05 M EDC (1:1 mixture) for 4 h at room temperature. The channel was incubated overnight in an antibody solution (100 μg/mL). Finally, after rinsing with PBS, the antigen (1 μg/mL) in PBS was flown through the microchannel in constant and in pulse mode using a syringe pump (PHD Ultra, Harvard Apparatus). Due to a leakage problem at higher flow rates, we limited our flow rates for the experiments up to 90 μL/min. We did not notice (using an optical microscope) any change in the microchannel geometry (height and width of the microchannel) for the flow rates used here.

2.5 Determination of capture efficiency

The solution of potassium ferrocyanide ($K_4[Fe(CN)_6]$) and potassium ferricyanide ($K_3[Fe(CN)_6]$, 1 mM (1:1)) in 10 mM (pH = 7.4) PBS solution (Imran et al. 2019; Bhuvana et al. 2013; Verma and Panda 2020) was used as the electrolyte. Platinum was used as the working and counter electrode and Ag/AgCl as a reference electrode (Zhang et al. 2019). The number of active sites (Kalita et al. 2012; Klink et al. 2011; Singh et al. 2011; Solanki et al. 2008; Chauhan et al. 2016) with respect to peak current was calculated utilizing the CV plot and the Brown–Anson model (Brown and Anson 1977) (the detailed information with sample calculation has given in the Supplementary Information). A larger decrease in the value of the peak current represents a lower number of active sites and this indicates a higher extent of reaction.

2.6 Flow characteristics using micro-PIV

To understand the pulse flow profile, the flow profiles inside the channel were characterized by micro-PIV (TSI, USA) at flow rates 30–90 μL/min (average 60 μL/min) and at different planes (bottom, an intermediate plane, and the mid plane). The results from the micro-PIV help in comparing the temporal variation in the streamlines (at 0.6 vector length-scale) at different flow conditions and help elucidate the role and significance of active mixing in generation of secondary flows. But due to the computational limitations, the dimensions of the microchannels used for experimental and simulations were different and, hence, a one-to-one comparison of the flow lines was not possible. This is the limitation for our study.

3 Results and discussion

3.1 Enhanced captured efficiency with pulsed flow

The effect of the nature of flow on the capture efficiency was studied experimentally using PSA/anti-PSA and also verified numerically. In Fig. 2, the experimental results of the percentage reduction of the peak current at $Re = 2.35$ for the constant and the pulse flow are shown on the left-hand side, and the simulation results of the average surface concentration at $Re = 0.48$, for the constant and the pulsed flow are shown on the right-hand side. In experiments, the magnitude of the reduction of peak current gives the extent of the reaction or the captured Ag; while in simulations, the amount of Ag captured is characterized in moles per unit area. We consider different values for Re (i.e., 0.48 and 2.35,
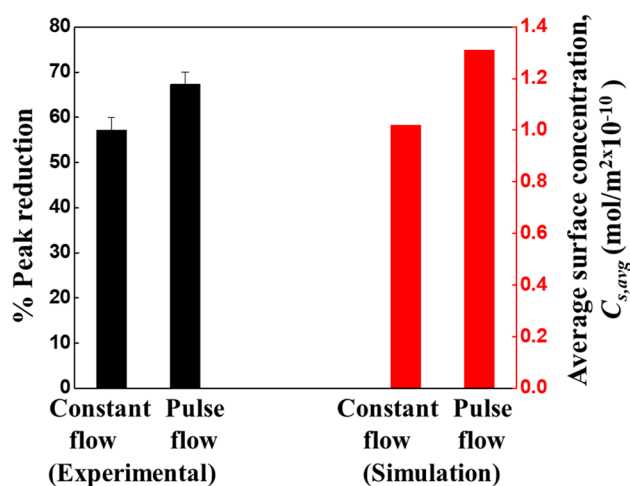
Fig. 2 The percentage reduction in peak current at Re = 2.35 with constant and pulsed flow (experimental) for the PSA/anti-PSA system and the average surface concentration ($C_{s,avg}$) at constant and pulsed flow at Re = 0.48 (simulation validation)

that is, different velocities for experiments and simulations) because the length of the microchannel is different for the experiments and the simulations. Due to computational limitations, we could not go beyond 3 mm and experimentally such small lengths (3 mm) do not provide sufficient signal to measure; hence, we chose longer (10-mm) microchannels. The average Sherwood number (Sh_{avg}) for the experiments and simulations were compared for the specific case—for experiments ($Sh_{avg} = 23.15$ at $Re = 2.35$, $Sc = 11,764.7$) and for simulations ($Sh_{avg} = 21.82$ at $Re = 1.2$, $Sc = 27,000$) (Subramanian; Wu et al. 2001). The values are comparable (i.e., within 6%). With the pulse flow conditions both in experiments (amplitude = 12.50 mm/s, $f = 0.05$ Hz, an average velocity = 60 (30–90) µL/min) and in simulations (amplitude = 2.50 mm/s, $f = 0.25$ Hz, an average velocity = 12 (6–18) µL/min), we observed an enhancement in the *capture efficiency*. For PSA/anti-PSA, using the previously described (Sect. 2.4) immunoassay protocol, the peak current obtained from the experiments after anti-PSA immobilization was 5.600 ± 0.208 µA. After PSA immobilization, the peak currents were 2.402 ± 0.079 µA and 1.831 ± 0.024 µA, for the constant and pulse flow, respectively. The reduction in the peak currents was $57.10 \pm 2.84\%$ and $67.29 \pm 2.65\%$ for the constant and pulse flow, respectively. In the case of pulse flow, a higher reduction in the peak current indicates a greater extent of reaction, when compared to constant flow. And in the case of the simulations, the average surface concentration (Cs,avg) was higher (29% more) for the pulse flow.

A dynamic PIV technique was used to characterize the flow in the pulse mode for which we had validated the no-slip condition for constant flow in our previous work (Verma and Panda 2020). Figure 3a illustrates the velocity as a function of time in the microchannel; while, Fig. 3b, c show the flow lines for the constant and pulse flow, respectively. The plane (for flow visualization) is 5 µm above the bottom surface of the channel. For constant flow, the flow lines are unidirectional; whereas for pulse flow, the flow lines are multidirectional (random circulation/distribution of streamlines). The presence of random and asymmetrical flow lines in the pulse flow improves the transport near the surface leading to better mixing than constant flow. Hart et al. (2010) had also discussed the enhancement of the heterogeneous immunoassays (using AC electroosmosis) near the electrode surface.

The pulse flow perturbs the bulk fluid and improves transport of the antigen molecule towards the microchannel surface. The presence of random movements and swirling motion of eddies improves the mixing locally, reduces the boundary layer thickness and enhances the *Ag* transport to the surface (Fig. 3c shows the flow lines near the bottom surface). At Re ~ 1 used in this study, the inertial forces cannot be neglected. In the pulsed flow here, the fluid packets respond to the change in the velocity obeying the principle

of mass conservation. This response is depicted in the randomness or the temporal variation of the flow lines. We have also calculated the Womersley number (W_0) which represents the ratio of transient inertial force to the viscous force ($Wo = L\sqrt{\omega/v}$) (Kumar et al. 2011). The calculated value of W_0 of about 0.06 which shows the viscous force dominates the flow (as $W_0 < 2$). This result is in agreement with Fujii et al. (2003), who demonstrated a better mixing performance using pulsed flow, and Yu et al. (2015), who obtained a higher signal intensity with the electrothermal effect at all concentrations of myeloperoxidase (MPO) used in their work. Thus, the results obtained here validate our observation that active mixing enhances the *capture efficiency*. The effects of different parameters on the *capture efficiency* are discussed in the subsequent sections.

3.2 Effect of velocity on capture efficiency

In pulsed flow, velocity, frequency, and amplitude affect the transport of *Ag* to the surface immobilized *Ab*. The effect of velocity is studied first, keeping amplitude (2.5 mm/s) and frequency (0.25 Hz) constant. Here, the flow is in the laminar regime with *Re in the range* 0.48–1.2, and the *St* in the range is 0.0005–0.0013.

The simulated values of the $C_{s,avg}$ are plotted on the z-axis as a function *Re* (a measure of velocity), and *St* in Fig. 4a. Re_0, *Re* and *St*, are the dimensionless numbers (Eqs. 13, 14, 15) useful in analysing the effect of pulse flow and its parameters. Re_o, a function of amplitude and frequency, is the measure of the mixing intensity. The amplitude and frequency are constant here; thus, the degree of mixing (Re_o) is constant. *St* is the ratio of the characteristic flow time to the characteristic pulsing time. In this case, the *Re* increases with the increase in the average velocity. The increased velocity reduces the residence time and thus *St* decreases which results in a decline in the propagation of the effective eddies (which keeps the fluid perturbed) and reduces the mixing extent. To see the combined effect of *Re* (increasing average velocity) and *St* (eddies propagation), i.e., increasing inertial forces and reducing eddies propagation (*St*) on average surface concentration ($C_{s,avg}$), we introduced a correlation among $C_{s,avg}$, *Re* and *St* (Fig. 4a) which is as follows:

$$C_{s,avg} = -3.3834 \times 10^{-10} + 6.8130 \times 10^{-10}Re - 2.0822 \\ \times 10^{-10}Re^2 + 2.5607 \times 10^{-7}St - 8.0792 \times 10^{-5}St^2. \tag{16}$$

The data points were fitted using a curve fitting tool (poly line) and the R^2 value was 0.99. The above correlation illustrates that the coefficient of *St* is higher than that of *Re*, indicating that the average surface concentration ($C_{s,avg}$) is dependent more on *St* than *Re*. This indicates that eddies propagation has a more capability to affect the
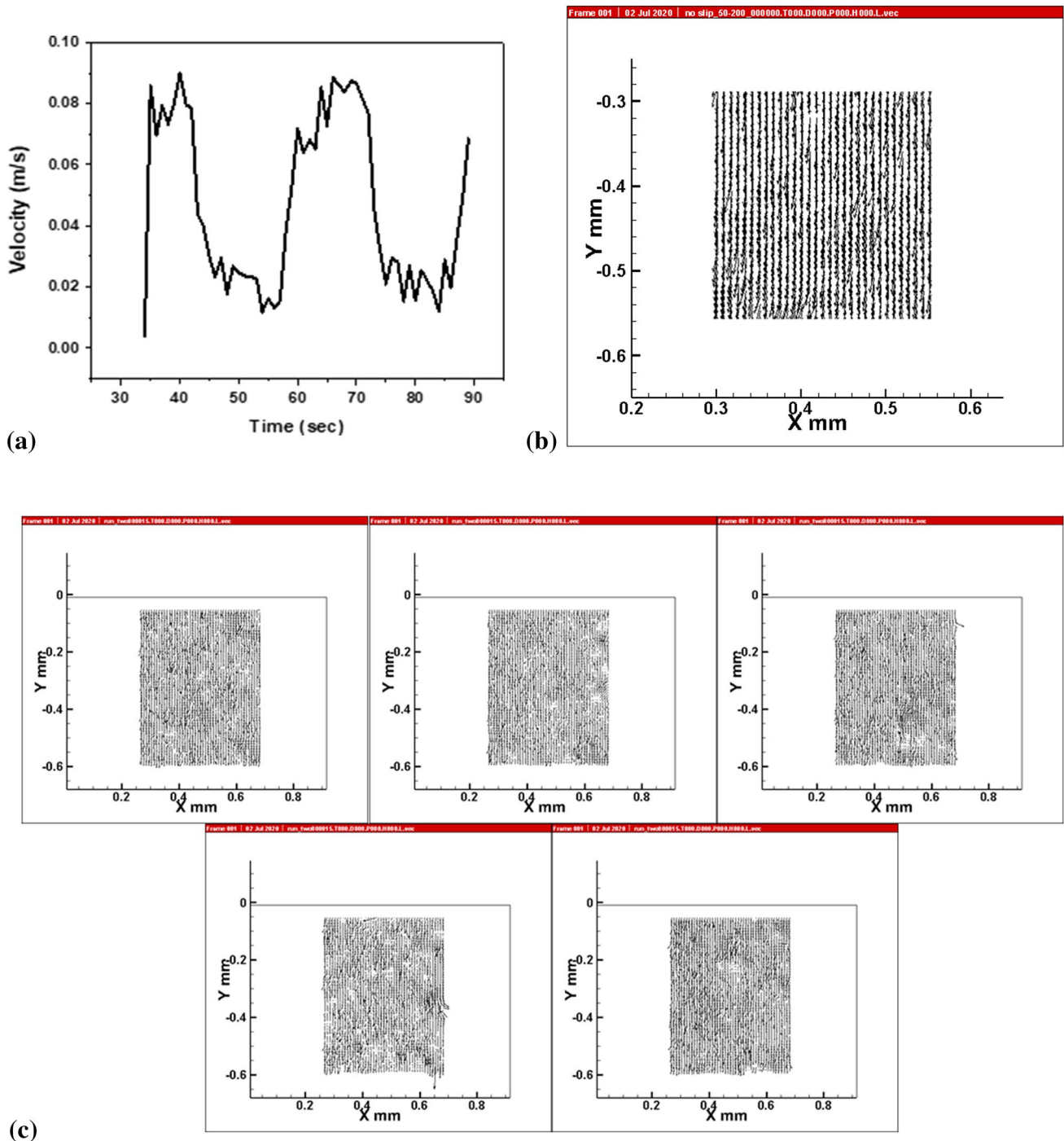
Fig. 3 Micro-PIV results for: **a** velocity (pulse nature) as a function of time at a chosen point in the microchannel, **b** constant flow, and **c** pulse flow near surface at different time stamps

capture efficiency of *Ag* than *Re* and elucidates the impact of active mixing on *capture efficiency*. Glasgow et al. (2004) also mentioned that the higher *St* lead to better mixing, while using the pulse flow for the mixing two fluids in the microchannel.

To understand better the 3D plot shown in Fig. 4a, we have divided it into two 2D plots: i) $C_{s,avg}$ as a function *Re,* Fig. 4b and ii) $C_{s,avg}$ as a function of *St,* Fig. 4c. In the range of *Re* studied (suitable for microfluidic immunosensors, $Re \sim 1$), it is seen that the capture efficiency increases monotonically with velocity. A similar behavior was reported
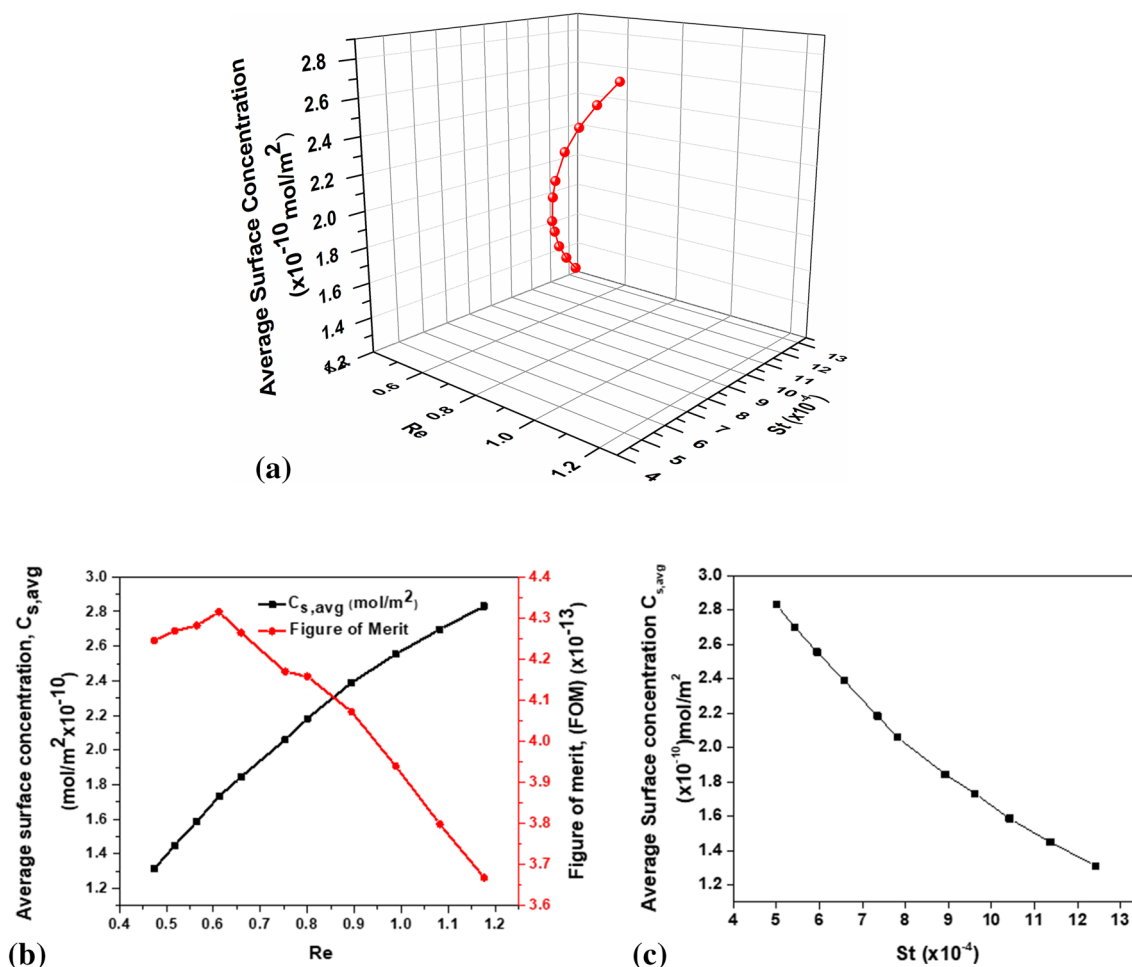
(a)

(b)

(c)

Fig. 4 **a** Correlation between $C_{s,avg}$, Re and St. **b** Simulated average surface concentration ($C_{s,avg}$) and figure of merit (FOM) as a function of Re, and **c** as a function of St, for pulsed flow

with a constant flow rate in our previous work (Verma and Panda 2020) and this was attributed to the reduction in the mass transfer boundary layer thickness. The lowering of the resistance to the mass transport can be seen as lowering of the characteristic time of transport (Rath and Panda 2015). However, at high values of *Re*, where the characteristic time of flow, i.e., (the residence time) will be low, lesser capture of the antigen is expected. Similar results were also seen by Alonso et al. (2014) and Cherkasov et al. (2020). Alonso et al. (2014) obtained a maxima in fluorescence signal (response) in *E. coli* detection and Cherkasov et al. (2020) obtained a maxima in the semi-hydrogenation (% conversion) of 2-methyl-3-butyn-2-ol (MBY) for the catalyst loading as a function of inlet velocity. Although, an increased velocity (within a range) facilitates a higher capture, it is associated with a higher pressure drop. Hence, a "figure of merit (*FOM*)", defined here as the ratio of the $C_{s,avg}$ to the pressure drop at a given flow rate, is calculated for the different conditions and plotted on the secondary *y*-axis in Fig. 4b. A maxima in the *FOM* was seen at *Re* = 0.6 (Mandal

et al. 2010, 2011; Singh et al. 2014 obtained either increasing or decreasing behavior in *FOM* for their improved coiled flow heat transfer system.). This indicates that higher *Re* can provide better analyte capture (the desired performance) but with a higher corresponding pressure drop. Figure 4c shows, the $C_{s,avg}$ as a function of *St* (at constant frequency and amplitude). At constant frequency and amplitude, the *St* decreases with the increase in the average velocity, i.e., *Re*. And we knew from above Fig. 4a that higher *Re* provide higher analyte capture. Thus, the increase in the $C_{s,avg}$ with the decrease in *St* again confirms the above-mentioned conclusion.

3.3 Effect of frequency

Frequency is an important parameter in the study of active mixing as it affects the characteristic time of the mass transport. Antigen capture depends on the interplay between transport, reaction, and geometrical parameters (Rath and Panda 2015). In this study, the geometry (straight
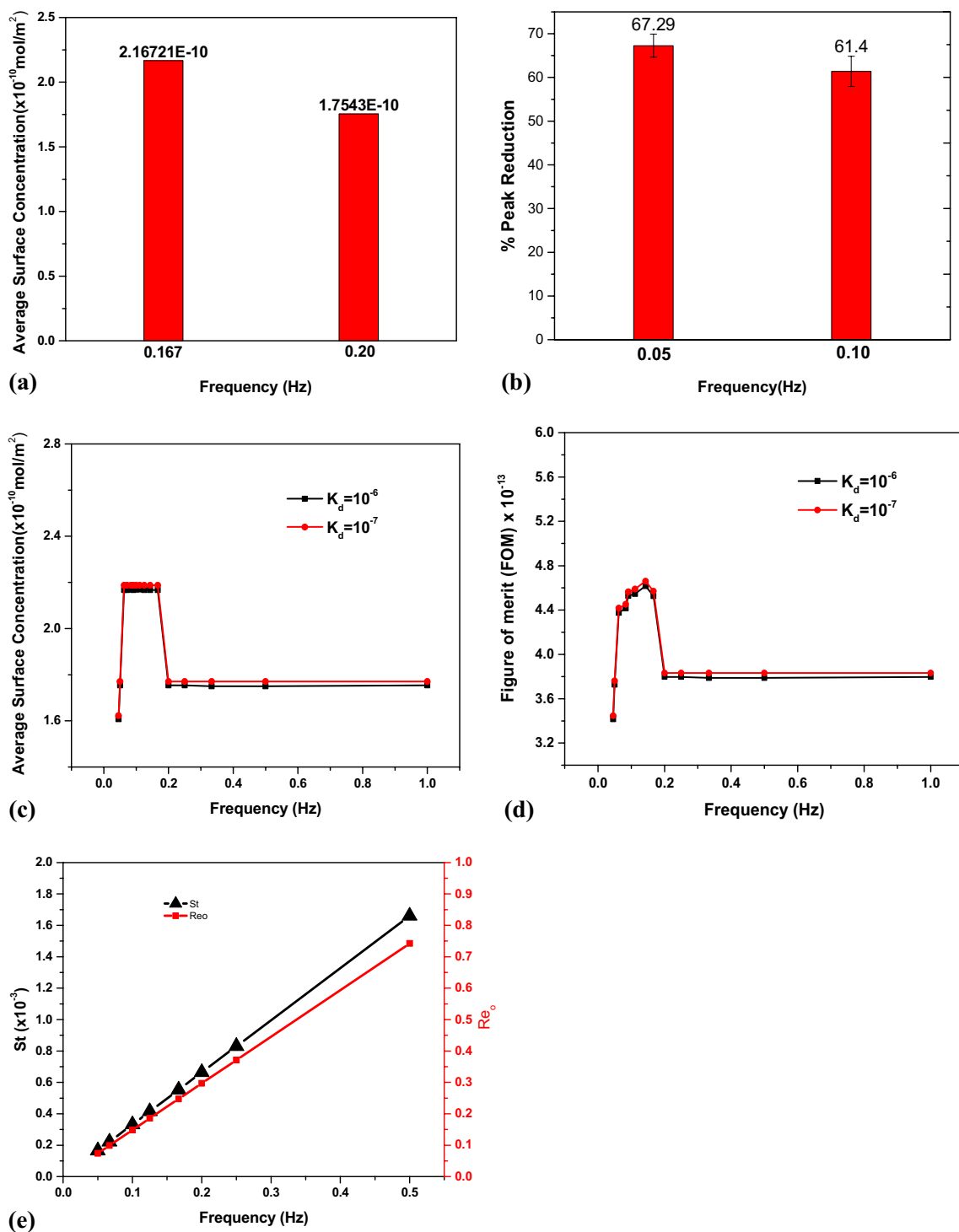
Fig. 5 **a** Average surface concentration ($C_{s,avg}$) at different frequencies at Re = 0.71 (simulation), **b** reduction in the peak current at Re = 2.35 at different frequencies (experimental validation) for PSA/anti PSA capture for frequency effect, **c** average surface concentration ($C_{s,avg}$) as a function of frequency, **d** figure of merit (FOM) of frequency, **e** Re_o and St as a function of frequency at Re = 0.71

microchannel) is the same for all the cases; hence, transport and reaction are the deciding factors for the extent of capture. Figure 5a shows $C_{s,avg}$ at two frequencies when Re = 0.71 (simulation), and Fig. 5b shows the reduction in

the peak current at Re = 2.35 for two frequencies (experimental validation) for PSA/anti-PSA. We have chosen different frequency ranges due to experimental and computational limitations (Similar to Sect. 3.2, we are validating here the

frequency effect empirically). We obtained a higher $C_{s,avg}$ (~24%) at $f = 0.167$ than at $f = 0.20$ in the simulations. In the experiments, the flow velocity was within a range of 30–90 µl/min (average 60 µl/min). The frequencies (f) were 0.05 Hz, and 0.10 Hz and the peak reduction was higher ($67.29 \pm 2.65\%$ at $f = 0.05$ and $61.40 \pm 3.45\%$ at $f = 0.10$) for the lower frequency. An increase in the frequency improves the transport up to a certain scale, but beyond that, it will not provide sufficient time to react and therefore, the capture decreases. This above result clarifies the fact, numerically as well as experimentally, that a higher frequency decreases the extent of the reaction and leads to reduced capture. Glasgow et al. (2004) had also observed a higher mixing (utilizing pulse flow) at lower frequencies due to greater contact time between the fluids. Similar effect of frequency was also observed by Fujii et al. (2003), Hart et al. (2010) and Chen et al. (2016), who obtained a relatively lower signal at higher frequencies. At a constant average velocity and amplitude, Re_0 and St (among Re, Re_0 and St) are a function of frequency only. The St increases with the increase in the frequency. However, at very high values of St, the fluid flow lines motion is so rapid, such that the species (Ag) does not have the sufficient time to reach the surface and bind with the Ab. Consequently, the performance is poorer than that achieved at lower values of St, and this finally leads to a reduced value of the $C_{s,avg}$.

To get more insight on the effect of frequency on the capture of Ag, the average velocity and the amplitude were kept at 7.53 mm/s and 2.51 mm/s, respectively. The frequency was varied over the range 0.045–1.0 Hz. Figure 5c presents $C_{s,avg}$ as a function of frequency at two values of K_d:10^{-6} and 10^{-7}. From Fig. 5c, it is observed that, initially for short span of frequency (0.0454–0.0625 Hz), the average surface concentration ($C_{s,avg}$) increases with the increase in frequency, and remains nearly constant for 0.0625–0.1667-Hz frequency range and decrease afterwards. A similar behavior was observed for both values of K_d. To explain this observation, two time scales were considered: one is the characteristic time of reaction and the other is the residence time scale, which are linked with the reaction and transport phenomena, respectively (Rath 2016). At lower frequencies, the reactive time $\geq$ residence time; while at higher frequencies, the fluid motion is rapid due to which the reactive time $<$ residence time which results in the lesser analyte capture. This result agrees with Chen and Cho (2008), who obtained the maxima in the extent of mixing as a function of St. A reason for the maxima being flat could be that we have considered many points in a small range (0.0454–0.0625 Hz), and the total frequency range is also small (0.0454–1); while other researchers have considered wider range of frequency. However, the pressure drop increases with frequency (for all values); hence, the FOM will also vary with frequency, which shown in Fig. 5d. The FOM also attains maxima as

a function of frequency and this pattern is the same for the both values of K_d. Such a behavior of frequency is not only limited to micro-range or to immunosensing applications; similar results were also obtained by Masngut and Harvey (2012) in butanol production in batch oscillatory baffled bioreactor at a higher Re_0 as a function of time. Figure 5e illustrates Re_o and St as a function of frequency. Re_o represents the mixing intensity, and it increases (linearly) with the frequency. At a higher mixing intensity, the eddies propagation is also more and enhances the transport. This explains the increasing behavior of Re_o and St with increased frequency.

In this section, we discuss the effect of frequency at a fixed plane with time. For pulse flow (in active mixing), the movement of the flow lines is random and time dependent. Figure 6a, b shows the flow profiles at different frequencies, and times and these pictures were selected where significant changes were seen. The direction of the flow lines at different times can be distinguished visually at various frequencies. We find that the direction of the flow lines are different at different times and turbulence is more at higher frequencies leading to improved transport but provides less time for reaction; hence, due to insufficient reaction time, the extent of capture decreases.

Until now, we have seen the effect of velocity at a constant frequency and the effect of frequency at constant velocity on the average surface concentration ($C_{s,avg}$). For a more detailed understanding, we extend our analysis and split the components of St. For a combined effect of frequency and velocity (Re), we varied the frequency (with range of 0.0667–0.50 Hz) and velocity ($Re = 0.52$–0.90) and conducted a numerical analysis. Figure 7 shows St as a function of frequency (0.0667–0.50) and velocity ($Re = 0.52$–0.90), and we obtain correlation ($R^2 = 0.964$) as follows:

$$St = 0.782 \times 10^{-3} - 1.102 \times 10^{-3} \times Re + 3.439 \times 10^{-3} \times f. \tag{17}$$

Figure 7 demonstrates a lower Re (i.e., velocity) and higher frequency for a higher value of St and validates that St is directly proportional to frequency (f) and inversely proportional to velocity (v). The correlation (Eq. 17) also indicates that frequency has a greater impact on St and effective eddy propagation because its coefficient is (about three times) higher than that of the velocity, thus, clarifying the impact of frequency on the St. In our earlier correlation also (Eq. 16), we found that frequency carries higher significance than velocity. Consequently, a high frequency with low velocity is considered to be a favorable combination for higher capture of Ag.

3.4 Effect of amplitude

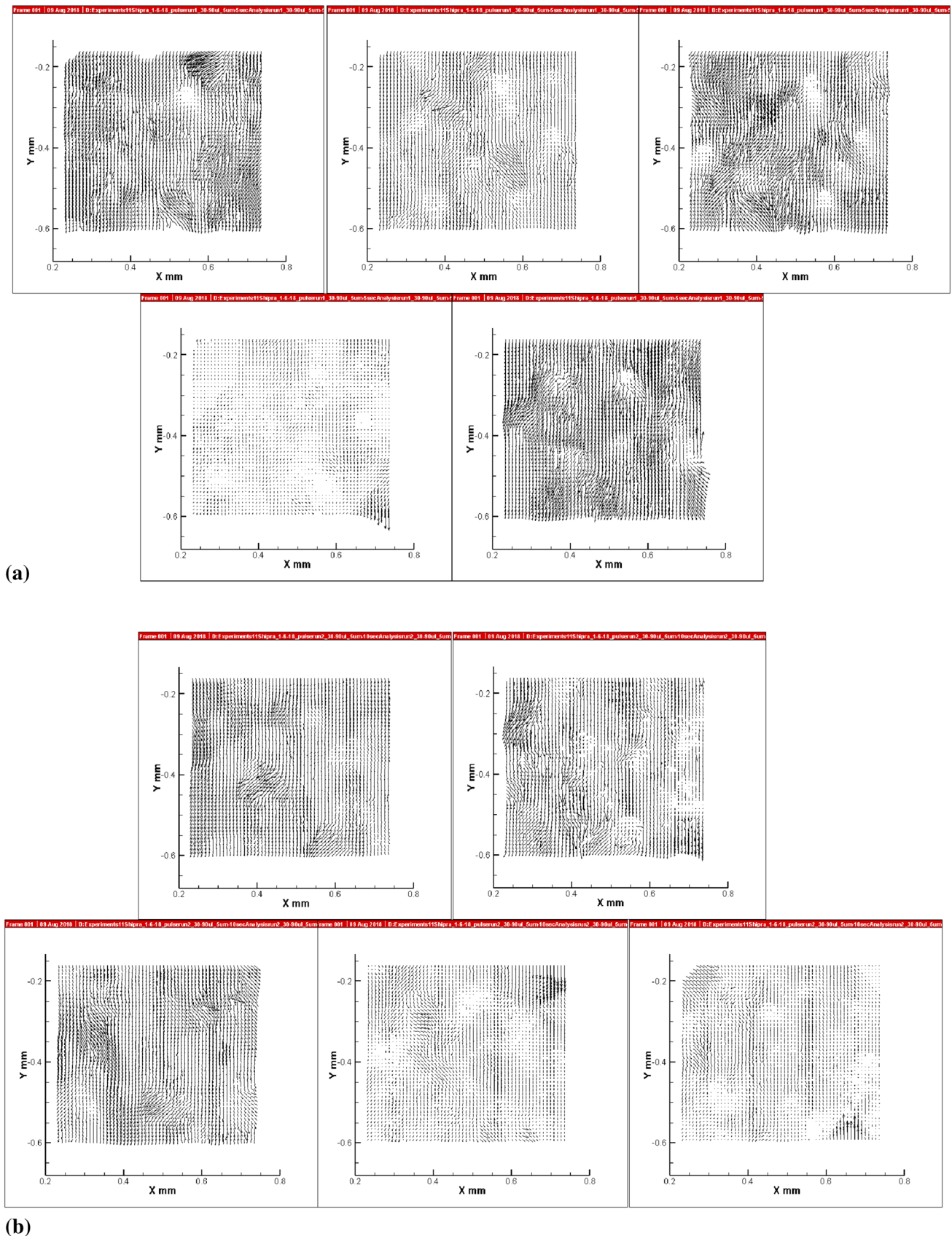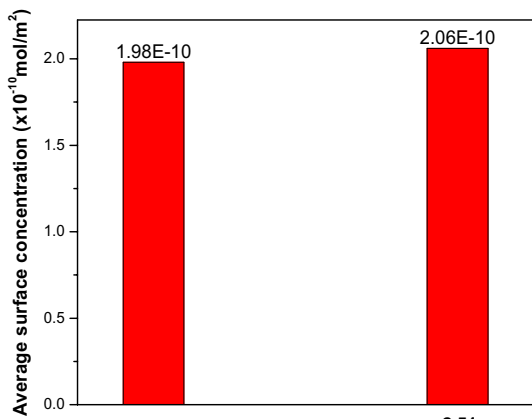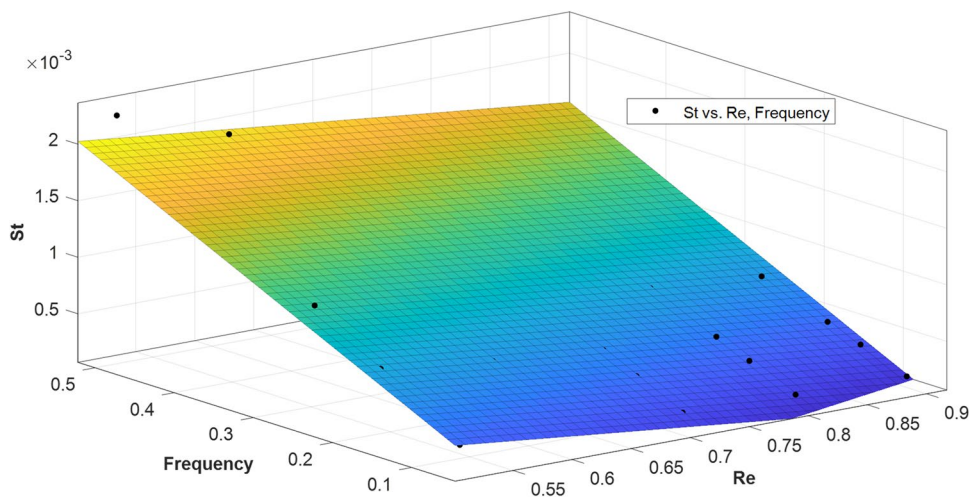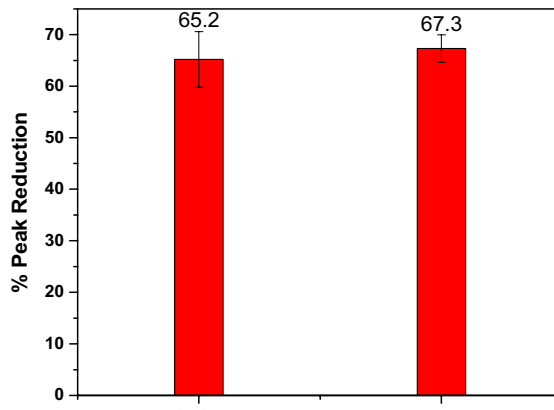The third key factor that affects the mass transfer is the amplitude of the pulse. To observe the effect of amplitude,

Fig. 6 Effect of frequency: Flow profile in the mid-plane at flow rate ranged 30–90 µl/min **a** $f = 0.1$ and **b** $f = 0.05$ Hz
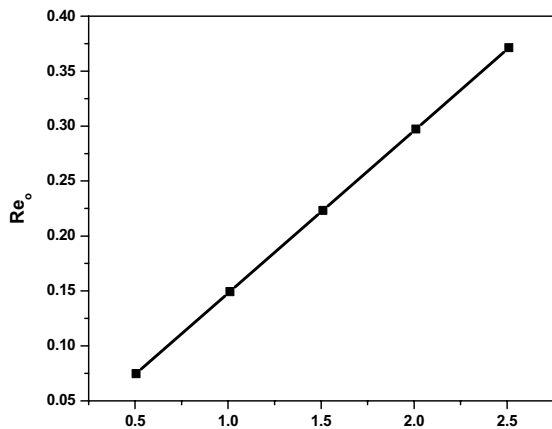
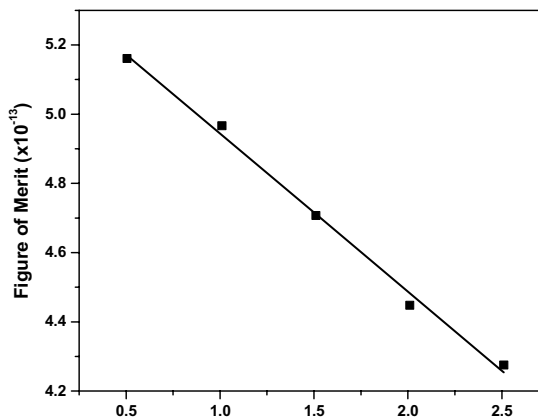**Fig. 7** St as a function of frequency (0.0667−0.50) Hz and velocity (Re = 0.52−0.90)

Fig. 8 **a** Average surface concentration ($C_{s,avg}$) at different amplitudes at Re = 0.71 (simulation), **b** reduction in the peak current at Re = 2.35 at different amplitudes (experimental validation) for PSA/anti PSA capture. **c** Re_o as a function of amplitude. **d** The figure of merit (FOM) as a function of amplitude

we fixed the frequency at 0.25 Hz and average velocity at 7.06 mm/s and varied the amplitude from 0.5 to 2.5 mm/s. Figure 8a shows $C_{s,avg}$ for different amplitudes at Re = 0.71

(simulation) and Fig. 8b shows the reduction in the peak current at Re = 2.35 for different amplitudes (experimental validation) for PSA/anti PSA capture. The response improves
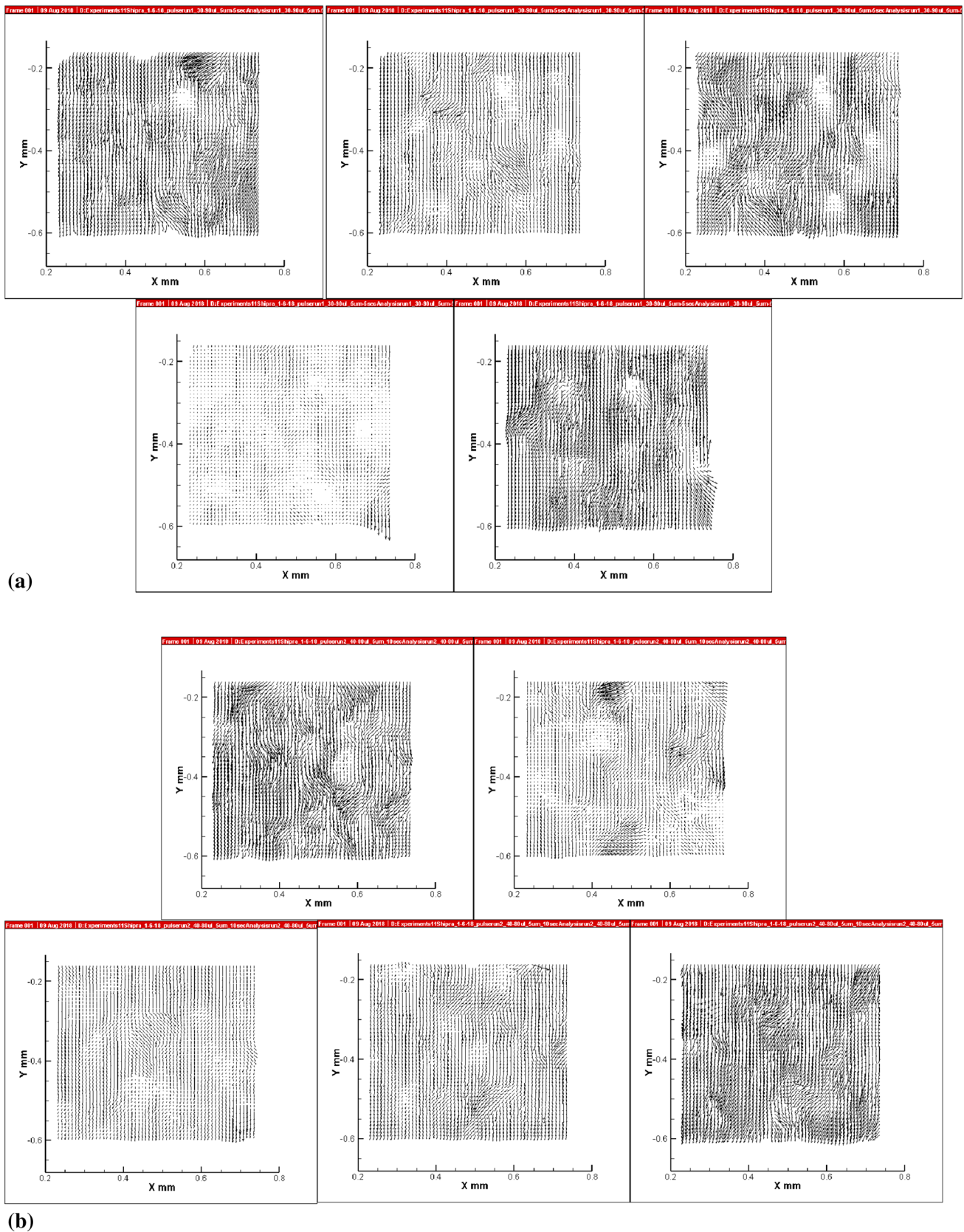
Fig. 9 Effect of amplitude, Flow profile in the mid-plane at f = 0.1 Hz **a** amplitude: 12.50 mm/s with corresponding flow rate ranged 30–90 μl/min, and **b** amplitude: 8.33 mm/s with corresponding flow rate ranged 40–80 μl/min

with the enhancement in the amplitude, but the impact is not as much as it is for velocity and frequency. In numerical studies, by increasing the amplitude from 2.01 mm/s to 2.51 mm/s (~25%), the enhancement obtained in $C_{s,avg}$ was just 4.04%. The experimental analysis also showed a similar behavior. In the experiments, the two distinct amplitudes were considered, and flow rates were ranged from 40 to 80 μl/min (amplitude = 8.33 mm/s) to 30–90 μl/min (amplitude = 12.50 mm/s), keeping the average flow rate was same (60 μl/min). We obtained a slight enhancement in the peak reduction (~2.1%) with higher amplitude. These results are in agreement with the Ni et al. (1994, 1995), who also obtained an enhanced mass transfer at higher amplitudes as a function of frequency.

Figure 8c shows Re_o as a function of amplitude and Fig. 8d shows the *figure of merit* (*FOM*) as a function of amplitude. With increasing amplitude, the flow lines move irregularly, and this enhances the Re_o, (the extent of mixing) and as a result, $C_{s,avg}$ also increases. However, at higher amplitudes, the pressure drop is also higher that leads to the decrease in the *FOM* value.

In Fig. 9a, b, the effect of amplitude on flow direction and mixing intensity is shown using micro-PIV. We selected those pictures where the substantial changes were visible. As the effect is not much visible, only slight enhancement in the capture can be observed. This section further validates the previously obtained experimental and numerical results of capture for different cases.

4 Conclusion

In this work, we have studied, both numerically and experimentally, the role of the active mixing in facilitating the transport of antigens in heterogeneous microfluidic immunosensors. The experiments on the capture of *PSA* by *anti-PSA* were conducted and the numerical simulations were used to verify the results. First, we checked the effect of the pulse flow on capture efficiency, and obtained an enhancement in the capture of the antigen. Subsequently, the study of active mixing parameter (average velocity, frequency and amplitude) on analyte capture was done. With the increase in the average velocity (u_{avg}), the antigen capture increases but the corresponding pressure drop also increases, and *FOM* attains a maxima at $Re \sim 0.6$. The analyte capture increases with the frequency also, but the increase in the frequency reduces the reaction time scale and decreases the capture of the analyte. The amplitude has the least effect on the antigen capture. The flow profiles were also seen with micro-PIV for the different cases to compare the temporal variation at various flow conditions. We also proposed two correlations among average the parameters $C_{s,avg}$, Re and St. The correlations indicate that dependency coefficient for St is higher than Re, and, thus, indicate that the vortex propagation has a higher effect (i.e., active mixing) on antigen capture efficiency than Re.

References

Abbott MSR, Harvey AP, Perez GV et al (2012) Biological processing in oscillatory baffled reactors: operation, advantages and potential. Interface Focus 3:1–13

Abbott MSR, Harvey AP, Perez GV et al (2014) Reduced power consumption compared to a traditional stirred tank reactor (STR) for enzymatic saccharification of alpha-cellulose using oscillatory baffled reactor (OBR) technology. Chem Eng Res Des 92:1969–1975

Alonso MB, Granados X, Faraudo J et al (2014) Magnetic actuator for the control and mixing of magnetic bead-based reactions on-chip. Anal Bioanal Chem 406:6607–6616

Art MS, Noblitt SD, Krummel AT et al (2018) IR-compatible PDMS microfluidic devices for monitoring of enzyme kinetics. Anal Chim Acta 1021:95–102

Asgharzadehahmadi S, Raman AAA, Parthasarathy R et al (2016) Sonochemical reactors: review on features, advantages and limitations. Renew Sustain Energy Rev 63:302–314

Bange A, Halsall B, Heineman WR (2005) Microfluidic immunosensor systems. Biosens Bioelectr 20:2488–2503

Bhuvana M, Narayanan JS, Dharuman V et al (2013) Gold surface supported spherical liposome–gold nano-particle nano-composite for label free DNA sensing. Biosens Bioelectr 41:802–808

Brown AP, Anson FC (1977) Cyclic and differential pulse voltammetric behavior of reactants confined to the electrode surface. Anal Chem 49:1589–1595

Chauhan R, Singh J, Solanki PR (2016) Label-free piezoelectric immunosensor decorated with gold nanoparticles: kinetic analysis and biosensing application. Sens Actuators B 222:804–814

Chen CK, Cho CC (2008) A combined active/passive scheme for enhancing the mixing efficiency of microfluidic devices. Chem Eng Sci 63:3081–3087

Chen Q, Wang D, Cai G et al (2016) Fast and sensitive detection of foodborne pathogen using electrochemical impedance analysis, urease catalysis and microfluidics. Biosens Bioelectr 86:770–776

Chen S et al (2019) Microfluidic device directly fabricated on screen-printed electrodes for ultrasensitive electrochemical sensing of PSA. Nano Res Lett 14:71

Chepyala R, Panda S (2013) Tunable surface free energies of functionalized molecular layers on Si surfaces for microfluidic immunosensor applications. Appl Surf Sci 271:77–85

Chepyala R, Panda S (2014) Zeta potential and reynolds number correlations for electrolytic solutions in microfluidic immunosensor. Micro Nano 18:1329–1339

Cherkasov N, Denissenko P, Deshmukh S et al (2020) Gas-liquid hydrogenation in continuous flow- The effect of mass transfer and residence time in powder packed-bed and catalyst-coated reactors. Chem Eng J 379:122292

Di CM, Ting YY, Yang DZ et al (2019) Microchannel with stacked microbeads for separation of plasma from whole blood. Chin J Anal Chem 47(5):661–668

From *MathWorld*– A Wolfram Web Resource. http://mathworld.wolfram.com/PiecewiseFunction.html. Accessed 22 Feb 2020

Fujii T (2002) PDMS-based microfluidic devices for biomedical applications. Micro Elec Eng 61–62:907–914

Fujii T, Sando Y, Higashino K et al (2003) A plug and play microfluidic device. Lab Chip 3:193–197

Glasgow I, Lieber S, Aubry N (2004) Parameters influencing pulsed flow mixing in microchannels. Anal Chem 76:4825–4832

Hart R, Lec R, Noh HM (2010) Enhancement of heterogeneous immunoassays using AC electroosmosis. Sens Actatuars B 147:366–375

Hessel V, Lowe H, Schonfeld F (2005) Micromixers—a review on passive and active mixing principles. Chem Eng Sci 60:2479–2501

Hu G, Gao Y, Li D (2007) Modeling micropatterned antigen-antibody binding kinetics in a microfluidic chip. Biosens Bioelectr 22:1403–1409

Ibii T, Kaieda M, Hatakeyama S et al (2010) Direct immobilization of gold-binding antibody fragments for immunosensor applications. Anal Chem 82:4229–4235

Imran H, Manikandan PN, Prabhu D et al (2019) Ultra selective label free electrochemical detection of cancer prognostic p53-antibody at DNA functionalized grapheme. Sens Biosens Res 23:100261

Kadilak AL, Ying L, Shrestha S et al (2014) Selective deposition of chemically- bonded gold electrodes onto PDMS microchannel side walls. J Electr Anal Chem 727:141–147

Kalita P, Singh J, Singh MK et al (2012) Ring like self-assembled Ni nanoparticles based biosensor for food toxin detection. Appl Phys Lett 100:093702

Kardous F, Fissi LE, Friedt JM et al (2011) Integrated active mixing and biosensing using low frequency vibrating mixer and Love-wave sensor for real time detection of antibody binding event. J Appl Phys 109(094701):1–8

Klink MJ, Iwuoha EI, Ebenso EE (2011) The electro-catalytic and redox-mediator effects of nanostructured PDMA-PSA modified-electrodes as phenol derivative sensors. Int J Electrochem Sci 6:2429–2442

Kumar H, Tawhai MH, Hoffmann EA et al (2011) Steady streaming: a key mixing mechanism in low-Reynolds-number acinar flows. Phys Fluids 23:041902-1–04190222

Lebedev K, Mafe S, Stroeve P (2006) Convection, diffusion and reaction in a surface-based biosensor: modeling of cooperativity and binding site competition on the surface and in the hydrogel. J Colloid Interface Sci 296:527–537

Lee CY, Chang CL, Wang YN et al (2011) Microfluidic mixing: a review. Int J Mol Sci 12:3263–3287

Mandal MM, Kumar V, Nigam KDP (2010) Augmentation of heat transfer performance in coiled flow inverter vis-a-vis conventional heat exchanger. Chem Eng Sci 65:999–1007

Mandal MM, Palka A, Nigam KDP (2011) Liquid_Liquid mixing in coiled flow inverter. Ind Eng Chem Res 50:13230–13235

Mansur EA, Mingxing YE, Yundong W et al (2008) A State-of-the-art review of mixing in microfluidic mixers. Chin J Chem Engg 16(4):503–516

Masngut N, Harvey AP (2012) Intensification of biobutanol production in batch oscillatory baffled bioreactor. Proc Eng 42:1079–1087

Nelson KE, Foley JO, Yager P (2007) Concentration Gradient Immunoassay. 1. An immunoassay based on interdiffusion and surface binding in a microchannel. Anal Chem 79:3542–3548

Nguyen NT, Wu Z (2005) Micromixers—a review. J Micromech Microeng 15:R1–R16

Ni X, Gao S, Pritchard DW (1994) A study of mass transfer in yeast in a pulsed baffled. Bioreactor Biotech Bioeng 45:165–175

Ni X, Gao S, Pritchard DW et al (1995) A comparative study of mass transfer in yeast for a batch pulsed baffled bioreactor and a stirred tank fermenter. Chem Eng Sci 50(13):2127–2136

Rath D, Panda S (2015) Enhanced capture efficiencies of antigens in immunosensors. Chem Eng J 60:657–670

Rath D, Panda S (2016) Correlation of capture efficiency with the geometry, transport, and reaction parameters in heterogeneous immunosensors. Langmuir 32:1410–1418

Rath D, Kumar S, Panda S (2012) Enhancement of antigen–antibody kinetics on nanotextured silicon surfaces in mixed non-flow systems. Mater Sci Eng C 32:2223–2229

Renaudin A, Chabot V, Grondin E et al (2010) Integrated active mixing and biosensing using surface acoustic waves (SAW) and surface plasmon resonance (SPR) on a common substrate. Lab Chip 10:111–115

Reverberi R, Reverberi L (2007) Factors affecting the antigen-antibody reaction. Blood Transfus 5:227–240

Sarvazyan A (2010) Diversity of biomedical applications of acoustic radiation force. Ultrasonics 50:230–234

Singh J, Kalita P, Singh MK et al (2011) Nanostructured nickel oxide-chitosan film for application to cholesterol sensor. Appl Phys Fluid 98:123702

Singh J, Choudhary N, Nigam KDP (2014) The thermal and transport characteristics of nanofluids in a novel three-dimensional device. Can J Chem Eng 92:2185–2201

Solanki PR, Kaushik A, Ansari AA et al (2008) Zinc oxide-chitosan nanobiocomposite for urea sensor. Appl Phys Lett 93:163903

Squires TM, Messinger RJ, Manalis SR (2008) Making it stick: convection, reaction and diffusion in surface-based biosensors. Nat Biol 26:417–426

Srivastava S et al (2011) A self assembled monolayer based microfluidic sensor for ures detection. Nanoscale 3:2971–2977

Subramanian RS Convective mass transfer. Department of Chemical and Biomolecular Engineering, Clarkson University. https://web2.clarkson.edu/projects/subramanian/ch330/notes/Convective%20Mass%20Transfer.pdf Accessed on 3 June 2020

Verma S, Panda S (2020) Correlations of the capture efficiency with the Dean number and its constituents in heterogeneous microfluidic immunosensors. Micro Nano 24:9

Vijayendran RA, Leckband DE (2001) A quantitative assessment of heterogeneity for surface-immobilized proteins. Anal Chem 73:471–480

Wang AW, Kiwan R, White RM et al (1998) A silicon-based ultrasonic immunoassay for detection of breast cancer antigens. Sens Actaturs B 49:13–21

Wu G, Datar RH, Hansen KM et al (2001) Bioassay of prostate-specific antigen (PSA) using microcantilevers. Biotech Nat 19:856–860

Yu C, Kim GB, Clark PM et al (2015) A microfabricated quantum dot-linked immuno-diagnostic assay (µQLIDA) with an electrohydro-dynamic mixing element. Sens Actaturs B 209:722–728

Zhang F et al (2015) A Microfluidic love-wave biosensing device for PSA detection based on an aptamer. Beacon Probe Sensors 15:13839–13850

Zhang D et al (2019) Electrochemical aptamer-based microsensor for real-time monitoring of adenosine in vivo. Anal Chimica Acta 1076:55–63